Research Square

Preprints are preliminary reports that have not undergone peer review.
They should not be considered conclusive, used to inform clinical practice,
or referenced by the media as validated information.

An Open-Source OpenSeesPy Framework for Simplified Micro-Modeling and OMA-Based Model Updating of Masonry Infill Walls under Cyclic Loading

Şevket ATEŞ

sates@ktu.edu.tr

Karadeniz Technical University

Adamou MAROU SEYNI SAMBEROU

Djibo Hamani University

Research Article

Keywords: masonry infill wall, simplified micro-modeling, cohesive interface, cyclic loading, operational modal analysis, model updating, OpenSeesPy

Posted Date: August 14th, 2026

DOI: https://doi.org/10.21203/rs.3.rs-10459935/v1

License: This work is licensed under a Creative Commons Attribution 4.0 International License.
Read Full License

Additional Declarations: No competing interests reported.

An Open-Source OpenSeesPy Framework for Simplified Micro-Modeling and OMA-Based Model Updating of Masonry Infill Walls under Cyclic Loading

Şevket ATEŞ[1, *], Adamou MAROU SEYNI SAMBEROU[2]

[1] *Department of Civil Engineering, Karadeniz Technical University, Trabzon, Türkiye*
[2] *Djibo Hamani University, Faculty of Agricultural Sciences, Tahoua, Niger*
[*] *Corresponding author: e-mail: sates@ktu.edu.tr*

Abstract

This paper presents a fully open-source, two-tier numerical investigation of the cyclic and dynamic behavior of masonry infill walls, implemented in OpenSeesPy and validated against a half-scale experimental campaign that combined FEMA 461 quasi-static tests and operational modal analysis (OMA). A simplified micro-model is adopted, in which the masonry units are expanded and the mortar joints together with the infill–frame boundary are reduced to cohesive–frictional zero-thickness interfaces; every constitutive parameter is traceable to the calibration of the reference study, so that the benchmark is reproducible without commercial software. In the first tier, a two-dimensional model of the specimen is driven through the displacement protocol and reproduces the measured peak lateral capacity of approximately 96 kN within 1.5%, together with the pinched hysteresis and the diagonal, corner-separation damage pattern observed in the test. In the second tier, a three-dimensional model with stabilized brick elements first resolves an ambiguity in the reported unit geometry—only a panel thickness of 185 mm reproduces the measured out-of-plane frequency, within 2%—and is then updated to the OMA frequencies by bound-constrained least squares. The updating Table 2 compares the updated model frequencies with the measurements. The updated model matches the three measured modes within +2.4%, −5.8%, and +12.1% (mean 6.8%) and identifies an effective in-plane infill–frame interface stiffness roughly five orders of magnitude below its cyclic-range value. This ratio provides a direct, experiment-based measure of the amplitude dependence of frame–infill interaction and implies that natural frequencies obtained from ambient vibration characterize the unlocked-contact state and should not be used to calibrate the stiffness entering seismic capacity models. The study thus delivers a reproducible open-source benchmark and demonstrates that separating the small- and large-amplitude regimes exposes interface behavior that a single-state calibration conceals.

Keywords: masonry infill wall; simplified micro-modeling; cohesive interface; cyclic loading; operational modal analysis; model updating; OpenSeesPy.

1. Introduction

Masonry infill walls are ubiquitous in steel and reinforced concrete frame construction, where they act as partitions and envelopes while simultaneously modifying the lateral stiffness, strength, and failure mechanisms of the bounding frames [1–3]. Post-earthquake reconnaissance and laboratory campaigns have repeatedly demonstrated that neglecting the frame–infill interaction may lead to unconservative estimates of drift demands and to the omission of infill-induced failure modes such as corner crushing, bed-joint sliding, and diagonal tension cracking [2, 3]. A reliable numerical description of this interaction is therefore a prerequisite both for the assessment of existing infilled frames and for the design of strengthening interventions.

Finite element idealizations of masonry are conventionally grouped into macro-models, in which the panel is homogenized or replaced by equivalent diagonal struts [2, 11], and micro-models, in which units and joints are represented explicitly [4–9]. The simplified micro-modeling strategy pioneered by Lourenço and Rots [5] and subsequently extended to cyclic and three-dimensional applications [6–9], expands the units by half the joint thickness and lumps the mortar and the two unit–mortar bond planes into a single zero-thickness interface governed by a cohesive traction–separation law. This strategy preserves the discrete crack pattern and the frictional character of masonry at a fraction of the cost of detailed micro-models, and it has become the reference approach for the in-plane cyclic analysis of infilled frames [6, 7, 9].

Within this line of research, a comprehensive experimental and numerical studies were carried out at Karadeniz Technical University on half-scale masonry walls and masonry-infilled steel frames. The experimental program of Samberou [12] combined FEMA 461 [18] quasi-static cyclic tests, operational modal analysis (OMA) under ambient excitation, and CFRP strengthening of hollow clay and solid clay brick walls. The companion numerical study of Samberou et al. [13] reproduced the tests with a three-dimensional simplified micro-model in ABAQUS, employing the Concrete Damaged Plasticity model [14, 15] for the units and surface-based cohesive contact for the joints, and reported load-bearing capacities and natural frequencies within 4% of the measurements. Notably, the highly nonlinear softening response of the interfaces obliged the authors to abandon the implicit solver in favor of an explicit quasi-static integration.

Two gaps motivate the present study. First, as emphasized in [13], published three-dimensional simplified micro-models frequently omit the information required to replicate them, and their

reliance on commercial explicit solvers obscures the relation between the interface parameters and the computed response. An open-source, fully scripted implementation in which every constitutive parameter is traceable to the calibration tables of the original experiments would render the benchmark reproducible and extensible. Second, the dynamic identification aspect of such specimens remains largely unexplored: the frequencies measured by OMA at micro-tremor amplitudes and the hysteretic response measured at drift levels three orders of magnitude larger probe two very different states of the frame–infill interfaces. The apparent contradiction between a bonded finite element model and the measured value of 12.6 Hz [12, 13] cannot be resolved by material calibration alone; it constitutes, instead, a model updating problem [20, 21] in which the effective small-amplitude interface stiffnesses and the participating apparatus mass are the unknowns.

In this paper, the experimental campaign of [12, 13] is revisited with a two-tier numerical strategy implemented entirely in the open-source OpenSeesPy framework [16, 17]. In the first tier, a two-dimensional simplified micro-model of the infilled steel frame is assembled from expanded elastic units, cohesive–frictional zero-thickness interfaces at bed joints, head joints, and the infill–frame boundary, and elastic beam–column elements for the pin-based test frame; the model is driven through the FEMA 461 displacement protocol and validated against the measured hysteresis, attaining the experimental peak load of approximately 96 kN within 1.5%. In the second tier, a three-dimensional model of the specimen is constructed with stabilized single-point-integration brick elements [23], and a sensitivity-based least-squares updating procedure [20, 24] is applied to the OMA frequencies. The updating identifies (i) an in-plane interface stiffness several orders of magnitude below its cyclic-range value, quantifying the amplitude dependence of the frame–infill contact, and (ii) an effective loading-apparatus mass consistent with the test setup. As a by-product, the modal analysis discriminates between two admissible readings of the reported unit geometry and confirms the wall thickness that reproduces the measured out-of-plane frequency within 2%.

The remainder of the paper is organized as follows. Section 2 presents the formulation: the interface constitutive laws and their finite element implementation, the infilled-frame model and loading protocol, and the eigenvalue analysis, mode classification, and model updating procedure. Section 3 describes the reference experiments. Section 4 reports the cyclic validation, Section 5 the modal identification and updating results, and Section 6 the conclusions.

2. Formulation

2.1. Simplified micro-model and interface constitutive laws

Following the simplified micro-modeling strategy [5, 9, 13], the masonry units are expanded by half the mortar thickness h_m in each direction, so that the panel geometry is preserved while the mortar joint and the two unit–mortar bond planes collapse into a single zero-thickness interface. The expanded units are discretized with plane-stress quadrilaterals (two-dimensional model) or stabilized single-point-integration brick elements [23] (three-dimensional model) and remain linear elastic; all material nonlinearity is lumped into the interfaces. Each interface integration point transmits a traction vector related to the separation vector through the diagonal elastic operator

$$t_n = K_{nn}\delta_n, \quad t_s = K_{ss}\delta_s \tag{1}$$

prior to damage, where the normal and tangential stiffnesses are obtained from the elastic moduli of unit (E_u, G_u) and mortar (E_m, G_m) and the physical joint thickness [9, 13]:

$$K_{nn} = \frac{E_u E_m}{h_m(E_u - E_m)}, \quad K_{ss} = \frac{G_u G_m}{h_m(G_u - G_m)} \tag{2}$$

In the finite element implementation, each coincident node pair along a joint is connected by a zero-length element whose uniaxial force–deformation laws are obtained by integrating the tractions over the tributary interface area A_i. In the opening mode (Mode I), the response is linear elastic up to the bond strength f_t and subsequently softens; the softening branch is scaled such that the dissipated work per unit area equals the Mode I fracture energy, which yields the characteristic ultimate opening

$$\delta_u^I = \frac{2G_f^I}{f_t} \tag{3}$$

while in compression the interface remains stiff and elastic (hard contact). In the sliding mode (Mode II), a Coulomb-type yield force combines cohesion and friction,

$$F_y = (c + \mu\,\sigma_n)\,A_i \tag{4}$$

with the normal stress σ_n evaluated from the gravity state, $\sigma_n(z) = \rho\, g\,(H - z) + \sigma_v$, in which ρ is the masonry density, H the panel height, and σ_v any external precompression. Post-peak, the shear branch softens toward a frictional residual with the ultimate sliding

$$\delta_u^{II} = \frac{2G_f^{II}}{c} \tag{5}$$

and the cyclic response is endowed with pinching, so that crack closure and the re-engagement of friction upon load reversal are represented. The mixed-mode interaction implicit in Eqs. (3)–

(5) is consistent with the quadratic initiation criterion and the Benzeggagh–Kenane propagation criterion [22] adopted in the reference ABAQUS model [13]. Head joints are assigned the same law with $\sigma_n = 0$, and the infill–frame boundary receives its own parameter set (stiffness, bond, cohesion, and friction coefficient) calibrated in [13] from diagonal compression tests of masonry triplets.

2.2. Infilled-frame model and loading protocol

The test frame which is two pin-based columns and a top beam is represented by elastic beam–column elements pin connected at the beam–column joints, with the measured section properties of the HEA200 profiles and the pinned supports of the experimental setup [12, 13]; the horizontal actuator, a pin-ended HEA200 strut driven by a hydraulic jack, imposes the lateral displacement at the beam centroid. The panel base is connected to the foundation through a bed-joint interface, and the lateral and top boundaries are tied to the frame through the infill–frame interfaces of Section 2.1. Gravity is applied first and held constant; the lateral loading then follows the FEMA 461 protocol [18], a displacement-controlled sequence of two cycles per amplitude with

$$u_{k+1} = 1.4\, u_k, \quad u_1 = 1.20\, mm \tag{6}$$

applied by displacement control with adaptive sub-stepping and a cascade of Newton-type algorithms. Because the interface laws soften, the implicit static solution may terminate at snap-back instabilities—precisely the difficulty that motivated the explicit integration in [13]; the base shear is monitored as the sum of horizontal reactions, and interface damage maps are constructed from the envelope of opening and sliding demands normalized by the elastic limits of Eqs. (3)–(5).

2.3. Modal analysis, mode classification, and model updating

For the dynamic tier, the undamped eigenvalue problem

$$(K - \omega_i^2 M)\, \varphi_i = 0 \tag{7}$$

is solved for the assembled infill–frame system, the mass matrix collecting the densities of the units, the mortar layers, the steel profiles, and the loading apparatus. Each mode is classified automatically from the energy content of its shape: with φ_x the in-plane and φ_y the out-of-plane components sampled on the frame columns and on the panel mid-surface, the symmetric and antisymmetric parts of φ_y with respect to the panel centerline separate torsional from out-of-plane shapes, and the mode is labeled in-plane translational, in-plane torsional, or out-of-plane according to the dominant energy. The lowest frequency of each class is paired with the

corresponding OMA target, the wall-dominance of the out-of-plane class being enforced so that local apparatus modes are excluded from the pairing.

The measured frequencies f'_i are identified from ambient vibration records by frequency domain decomposition [19]. Because ambient excitation probes the interfaces at micro-tremor amplitudes, their effective stiffnesses differ from the cyclic-range values of Section 2.1; they are therefore treated, together with the effective apparatus mass, as the updating parameters

$$\theta = [\, s_x \,, s_y \,, M_{ap} \,] \tag{8}$$

where s_x and s_y scale the in-plane and out-of-plane infill–frame interface stiffnesses and M_{ap} is the loading-apparatus mass, guided transversely by the actuator axis. The updated parameters minimize the weighted frequency residuals

$$\theta^* = arg\ min\ \frac{1}{2}\Sigma_i\left(\frac{f_i(\theta) - f_i}{f_i}\right)^2 \tag{9}$$

solved with the bound-constrained trust-region-reflective least-squares algorithm [24] on the logarithms of the stiffness scales, each function evaluation entailing a full model reassembly and eigen-solution. The formulation deliberately separates the two regimes: the cyclic tier employs the laboratory-calibrated interface parameters of [13], whereas the updated parameters of Eq. (9) characterize the small-amplitude state of the same interfaces; the ratio between the two constitutes a direct, experiment-based measure of the amplitude dependence of frame–infill interaction.

2.4. Numerical implementation in OpenSeesPy

Both tiers of the methodology are implemented as single-file, fully parameterized Python scripts in OpenSeesPy [17], the Python interpreter of the OpenSees finite element framework [16]. All geometric, material, and interface quantities of Sections 2.1–2.3 appear once, in a declarative input block at the head of each script, so that every number entering the analyses is traceable to the calibration tables of the reference study [13] and the models can be reproduced, audited, or extended without access to commercial software. The mentioned model given in Figure 1.

In the cyclic tier, the panel occupies a two-dimensional, two-DOF-per-node subdomain. Each expanded unit is meshed with plane-stress `quad` elements on a half-unit grid whose nodes are deliberately duplicated across joint lines, so that every bed-joint, head-joint, and boundary interface reduces to pairs of geometrically coincident nodes. Each pair is connected by a `zeroLength` element carrying two uniaxial materials, one per local direction. The traction–

separation laws of Eqs. (1)–(5) are realized with the multilinear `Hysteretic` material: in the normal direction, a trilinear tensile branch peaks at the bond force $f_t A_i$ and softens over the Mode I opening of Eq. (3), while the compressive branch remains stiff and elastic, emulating hard contact; in the tangential direction, a symmetric trilinear envelope yields at the Coulomb force of Eq. (4), softens over the Mode II sliding of Eq. (5) toward a frictional residual, and is assigned pinching factors (`pinchX` = 0.8, `pinchY` = 0.3) so that crack closure and the re-engagement of friction upon reversal are reproduced. Interface forces are obtained from the tractions by tributary-area integration along each joint, with coincident duplicates sharing the tributary area.

The steel frame is assembled in a coexisting three-DOF-per-node subdomain from `elasticBeamColumn` elements with the measured section properties, pinned column bases, and rigid beam–column joints. The mixed-DOF coupling between frame and panel is effected through companion nodes: at every attachment point a two-DOF node is created at the frame-node location, slaved to its translations by `equalDOF`, and connected to the adjacent panel node by the interface `zeroLength` element, so that the infill–frame constitutive law of Table 1 acts between the two subdomains without constraint conflicts. Constraints are handled by the transformation method, equations are ordered by reverse Cuthill–McKee, and the sparse system is solved with UMFPACK.

The loading history follows the two-stage scheme of Section 2.2. Gravity is applied under load control in ten increments and locked by resetting the pseudo-time; the FEMA 461 protocol of Eq. (6) is then imposed by displacement control at the beam-level control node with a 0.05 mm increment. Convergence is monitored on the displacement-increment norm (tolerance 10^{-6}); upon local failure the solver escalates automatically through Krylov-accelerated Newton, Newton with line search, and modified Newton iterations with relaxed tolerances, and, if necessary, subdivides the increment adaptively before restoring the reference settings. The base shear is recovered at every converged step as the sum of horizontal support reactions, and interface damage maps are assembled from the envelopes of the `zeroLength` deformations—opening and sliding demands normalized by the elastic limits of Eqs. (3)–(5)—queried at the peak of every protocol amplitude.

In the dynamic tier, the panel is discretized with `SSPbrick` elements [23]—stabilized single-point-integration hexahedra that are locking-free at the aspect ratios imposed by the thin mortar layers—arranged in alternating unit and mortar courses with their respective elastic constants and densities, the consistent nodal masses deriving directly from the material densities. The

frame occupies a six-DOF beam subdomain coupled to the solid mesh by the same companion-node construction, the loading apparatus enters as a lumped, transversely guided mass at beam level, and the infill–frame interfaces carry elastic `zeroLength` springs whose stiffnesses are the updating unknowns of Eq. (8). The eigenproblem of Eq. (7) is solved with the built-in Arnoldi solver (with a dense generalized solver as fallback), and the mode classification of Section 2.3 is evaluated from the nodal eigenvectors sampled on the panel mid-surface and on the columns. The updating of Eq. (9) is driven by the trust-region-reflective least-squares algorithm [24] operating on the logarithms of the stiffness scales; each residual evaluation entails a complete model reassembly and eigen solution.

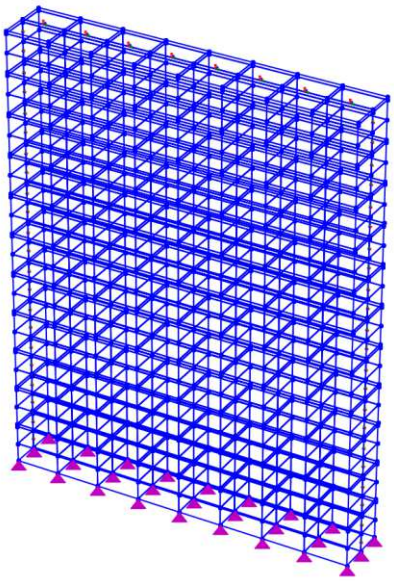


Figure 1. OpenSeesPy model

2.5. Algorithm structure and key implementation details

The overall organization of the two tiers is summarized in the flowchart of Figure 2. Both branches share a single declarative input block; the left branch performs the displacement-controlled cyclic analysis, and the right branch performs the eigenvalue-based model updating. The two decision diamonds embody the only iterative constructs of the procedure: the inner convergence loop of the static solver, with its automatic algorithm cascade, and the outer least-squares loop of the updating. The remainder of this subsection documents the four constructs that are essential to reproducing the results—the interface material generators, the mixed-DOF frame–panel coupling, the robust displacement-controlled driver, and the eigen-solution-in-the-loop of the updating—by reproducing the governing code fragments.

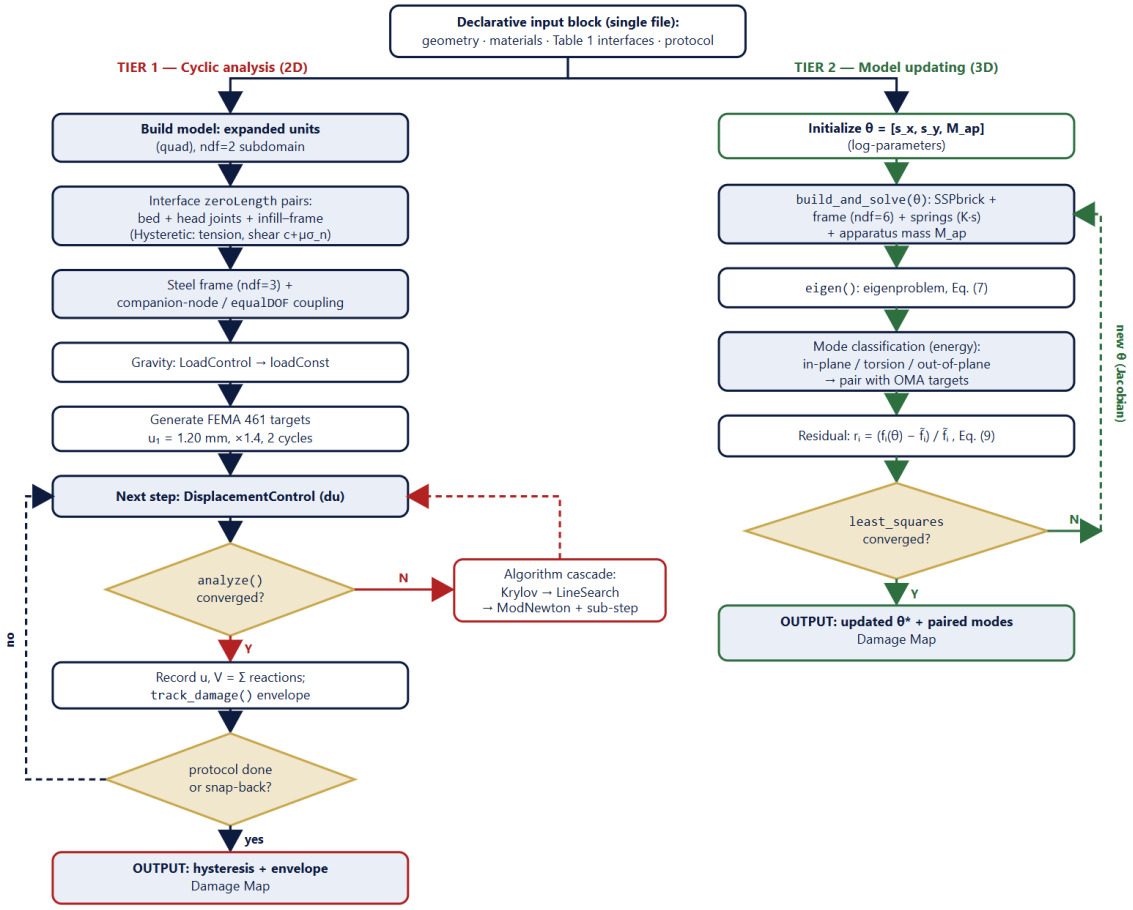


Figure 2. Flowchart of the two-tier OpenSeesPy strategy: cyclic analysis (left) and OMA-based model updating (right).

2.5.1. Interface material generators

Each joint direction is produced by a small factory that converts the physical interface parameters of Table 1 and the tributary area A_i into an OpenSees `Hysteretic` uniaxial material. In the normal direction (Listing 1), the tensile envelope peaks at the bond force and softens over the Mode I opening of Eq. (3), while the compressive branch is kept stiff to emulate hard contact; in the tangential direction the yield force follows the Coulomb law of Eq. (4), evaluated on the gravity normal stress passed as `sn`, and softens over the Mode II sliding of Eq. (5), with the pinching pair (0.80, 0.30) governing crack closure on reversal.

Listing 1 Normal (Mode I) and tangential (Mode II) interface materials.

```
def normal_malzeme(A, Knn, ft, GfI):        # Mode-I (opening)
    k  = Knn*A
    d1 = ft*A/k                              # bond-force peak
    du = max(2.0*GfI/ft, 3.0*d1)             # Eq.(3): 2 Gf_I / f_t
    ops.uniaxialMaterial('Hysteretic', m,
        ft*A, d1, 0.08*ft*A, du, 0.05*ft*A, 3*du,   # tensile softening
       -k*0.020,-0.020, -k*0.030,-0.030, -k*0.040,-0.040, # stiff compr.
        1.0, 1.0, 0.0, 0.0, 0.0)
```

```
def kayma_malzeme(A, Kss, c, sn, mu, du_pl): # Mode-II (sliding)
    Fy = (c + mu*max(sn, 0.0))*A            # Eq.(4): Coulomb yield
    dy = Fy/(Kss*A)
    ops.uniaxialMaterial('Hysteretic', m,
        Fy,dy, 0.55*Fy,du, 0.30*Fy,3*du,
       -Fy,-dy,-0.55*Fy,-du,-0.30*Fy,-3*du,
        0.80, 0.30, 0.0, 0.0, 0.0)          # pinchX, pinchY
```

2.5.2. Mixed-DOF frame–panel coupling

The panel is built in a two-DOF-per-node model, whereas the steel frame requires rotational degrees of freedom and is therefore built in a coexisting three-DOF model. The two are joined without constraint conflict by a companion node placed at each frame attachment point, slaved in translation to the frame node with `equalDOF` and connected to the adjacent panel node by the interface `zeroLength` element (Listing 2). The local direction ordering distinguishes the vertical column faces (normal along `x`) from the top beam interface (normal along `y`).

Listing 2 Companion-node construction for the infill–frame interface.

```
def es_dugum(fr_nd, x, y):                  # companion 2-DOF node
    ops.model('basic','-ndm',2,'-ndf',2)
    nd = yeni_dugum(x, y)
    ops.model('basic','-ndm',2,'-ndf',3)
    ops.equalDOF(fr_nd, nd, 1, 2)           # slave translations
    return nd

es = es_dugum(fr_nd, x, y)                  # panel<->frame spring
mN = normal_malzeme(A, Knn_bf, tn_bf, GfI_bb)
mS = kayma_malzeme(A, Kss_bf, ts_bf, 0.0, mu_bf, du_bf)
if yon in ('sol','sag'):                    # column face
    ops.element('zeroLength', e, es, duvar_nd, '-mat', mN, mS,
                '-dir', 1, 2)
else:                                       # beam soffit
    ops.element('zeroLength', e, es, duvar_nd, '-mat', mS, mN,
                '-dir', 1, 2)
```

2.5.3. Robust displacement-controlled driver

The FEMA 461 targets are traversed by displacement control. When a step fails, the driver escalates through a cascade of Newton-type algorithms with relaxed tolerances before restoring the reference settings; persistent failure—characteristic of the snap-back that terminates the softening response—breaks the loop and preserves the converged history (Listing 3). The base shear is recovered from the horizontal reactions, and the interface damage envelopes are updated at each amplitude peak.

Listing 3 Displacement-controlled step with automatic algorithm cascade.

```
ops.integrator('DisplacementControl', kontrol, 1, du)
for _ in range(npts):
```

```
    ok = ops.analyze(1)
    if ok != 0:                              # algorithm cascade
        for alg in ['KrylovNewton','NewtonLineSearch',
                    'ModifiedNewton']:
            ops.algorithm(alg)
            ops.test('NormDispIncr', 1e-5, 300)
            ok = ops.analyze(1)
            if ok == 0: break
        ops.algorithm('Newton')              # restore reference
        ops.test('NormDispIncr', 1e-6, 80)
        if ok != 0:                          # snap-back -> stop
            derz_izle(); break
    u_k.append(ops.nodeDisp(kontrol, 1))
    V_k.append(taban_kesme())                # -Sum horiz. reactions
```

2.5.4. Eigen-solution in the updating loop

In the dynamic tier, the objective passed to the bound-constrained least-squares solver [24] rebuilds the entire model for a trial parameter vector, solves the eigenproblem of Eq. (7), classifies the modes by the energy content of their shapes, and returns the normalized frequency residuals of Eq. (9). Because each evaluation is a complete reassembly and eigensolution—fast for a model of this size—the full identification converges in a few tens of seconds (Listing 4).

Listing 4 Model reassembly, eigen-solution, and residual for the updating.

```
def kur_ve_coz(s_ara_x, s_ara_y, M_ap):     # rebuild + eigen
    ...                                      # SSPbrick + frame + springs
    lam  = ops.eigen(numModes)               # Eq.(7)
    frek = [sqrt(l)/(2*pi) for l in lam]
    # classify each mode: in-plane / torsion / out-of-plane
    # from u_x and symmetric/antisymmetric u_y energy
    return f3                                # paired class frequencies

def artik(p):                                # residual vector, Eq.(9)
    f3 = kur_ve_coz(10**p[0], 10**p[1], p[2])
    return (f3 - f_hedef) / f_hedef

coz = least_squares(artik, p0,               # trust-region-reflective
        bounds=([-5,-5,0.05], [0.5,0.5,6.0]))
```

Together, the four listings expose every non-trivial modeling decision behind the results of Sections 4 and 5; the complete scripts, which differ from these fragments only in bookkeeping (node/element tagging, tributary-area accounting, and figure generation), are available as noted in Section 2.4.

2.6. Constitutive model of the masonry interface

In the simplified micro-modeling strategy the masonry units are treated as linear-elastic continua and the entire nonlinearity of the wall—cracking, sliding, dilatant friction, and the cyclic degradation that accompanies them—is concentrated at the joints. The fidelity of the

model therefore rests almost entirely on the constitutive law assigned to the interfaces. This section sets out that law: its mechanical basis in cohesive-zone and Coulomb-friction theory, the way it is realized in OpenSeesPy through uniaxial materials attached to zero-length elements, the calibration of its parameters from the reference experiments, and its scope and limitations relative to the plasticity-based interface models of the masonry literature.

2.6.1. Mechanical basis: cohesive traction–separation and frictional sliding

A masonry joint transmits load through two coupled mechanisms. Normal to the bed, it behaves as a cohesive crack: it carries tension up to the bond strength f_t, after which micro-cracking coalesces and the transmissible traction decays with increasing opening, the area under the traction–separation curve equalling the Mode I fracture energy G_f^I. Tangential to the bed, it behaves as a frictional contact obeying a Coulomb criterion: sliding initiates when the shear traction reaches the sum of a cohesive term and a frictional term proportional to the compressive normal stress, and the shear capacity likewise degrades over a Mode II fracture energy G_f^{II}. In the elastic range the two directions are uncoupled and governed by the interface stiffnesses of Eq. (2), so that the traction vector and the separation vector are related by Eq. (1). Damage initiation follows the quadratic stress criterion, and propagation the Benzeggagh–Kenane mixed-mode law, exactly as in the reference model [13]:

$$\left(\frac{t_n}{t_n^{max}}\right)^2 + \left(\frac{t_s}{t_s^{max}}\right)^2 = 1 \tag{10}$$

This continuum-mechanical picture—elastic traction–separation, strength envelope, energy-regularized softening—is the target that the OpenSeesPy realization approximates with uniaxial components, as described next.

2.6.2. Realization in OpenSeesPy: uniaxial materials on zero-length elements

OpenSees does not provide a single built-in cohesive-frictional interface element for masonry; instead, the joint is assembled from a `zeroLength` element connecting two coincident nodes, to which one uniaxial material is assigned per local direction (normal and tangential). The interface tractions of Section 2.6.1 are converted to forces by multiplying by the tributary interface area A_i, so that each uniaxial law operates on a force–deformation pair ($F_{n,s}, \delta_{n,s}$). The multilinear `Hysteretic` uniaxial material is used for both directions, because it offers exactly the ingredients the joint requires: a user-defined trilinear backbone in each sense of loading, and a set of parameters governing unloading/reloading stiffness degradation and pinching under cyclic reversal.

The `Hysteretic` backbone is specified by three points per sense (a peak and two post-peak points), together with the pinching factors p_x and p_y, the stiffness-degradation parameters d_1, d_2 (linked to ductility), and an energy-based degradation parameter β. Its call signature is

```
uniaxialMaterial('Hysteretic', tag,  s1p,e1p, s2p,e2p, s3p,e3p,
                 s1n,e1n, s2n,e2n, s3n,e3n,  pinchX,pinchY, damage1,damage2, beta)
```

Normal direction. The tensile sense of the backbone is a cohesive law: the first point is the bond force at first cracking, $F_t = f_t A_i$, reached at the elastic opening $\delta_1 = F_t / (K_{nn} A_i)$; the two post-peak points impose a softening branch whose extent is fixed by the Mode I fracture energy, giving the characteristic ultimate opening

$$\delta_u^I = \frac{2\, G_f^I}{f_t} \tag{11}$$

The compressive sense is assigned a stiff, essentially elastic branch of high slope and negligible strength decay, so that the joint transmits compression without interpenetration—the uniaxial surrogate for the hard-contact condition of the continuum model. Because masonry crushing is not the governing mechanism for the in-plane wall considered here (failure is by joint cracking and sliding), this representation of compression is adequate; where unit crushing matters, a compressive cap would be added to the backbone.

Tangential direction. The shear backbone is a Coulomb law. Its yield force combines cohesion and friction on the current normal stress σ_n:

$$F_y = (\, c + \mu\, \sigma_n \,)\, A_i \tag{12}$$

attained at the elastic slip $\delta_y = F_y / (K_{ss} A_i)$; the post-peak points soften the shear capacity toward a frictional residual over the Mode II sliding

$$\delta_u^{II} = \frac{2\, G_f^{II}}{c} \tag{13}$$

The backbone is defined symmetrically in the two senses of shear so that the joint responds identically to forward and reversed sliding. The normal stress entering Eq. (12) is taken from the gravity state, $\sigma_n(z) = \rho\, g\, (\, H - z\,) + \sigma_v$; the consequences of this simplification are discussed in Section 2.6.4.

Cyclic rules. Under load reversal the `Hysteretic` material reproduces the two phenomena that dominate the cyclic response of masonry joints. Pinching, controlled by p_x and p_y, represents the low tangent stiffness that prevails while a previously opened joint re-closes, before contact is re-established and friction re-engages; values of $(\, p_x, p_y\,) = (\, 0.80, 0.30\,)$ are used here.

Stiffness degradation, through d_1, d_2, reduces the reloading stiffness with accumulated deformation; the energy term β is left inactive so that degradation is ductility-driven rather than energy-driven. The composite force–deformation response of a joint is thus

$$F_s(\delta_s) = Hysteretic[\, F_y, \delta_y, \delta_u^{II};\ p_x, p_y, d_1, d_2\,] \tag{14}$$

with the analogous expression in the normal direction. Two material tags are generated per joint—one normal, one tangential—and attached to the `zeroLength` element in the corresponding local directions; the head joints receive the same laws with $\sigma_n = 0$, and the infill–frame boundary receives its own parameter set (Table 1).

2.6.3. Parameter calibration

Every quantity entering Eqs. (10)–(13) is fixed from the calibration of the reference experimental study [13], so that no parameter is free. The elastic stiffnesses follow from the unit and mortar moduli through Eq. (2); the bond strength, cohesion, and friction coefficient are those obtained from diagonal-compression tests of masonry triplets; and the fracture energies are the standard values adopted in [13]. Table 1 collects the values used for the brick–brick and infill–frame interfaces and maps each to the `Hysteretic` backbone quantity it defines.

Table 1. Interface model parameters and their role in the Hysteretic backbone.

Parameter	Brick–brick	Infill–frame	Role in backbone
Normal Stiffness K_{nn} (N/mm³)	70	11	normal elastic slope, Eq. (2)
Shear Stiffness K_{ss} (N/mm³)	40	11	shear elastic slope, Eq. (2)
f_t (MPa)	0.23	0.10	tensile peak $F_t = f_t A_i$
Bond strength t_n (MPa)	0.23	0.10	Interface model parameters
Cohesion c (MPa)	0.15	0.15	shear cohesion in Eq. (12)
Friction coefficient μ	0.75	0.57	friction coefficient, Eq. (12)
G_f^I (N·mm/mm²)	0.025	—	Mode I softening, Eq. (11)
G_f^{II} (N·mm/mm²)	0.50	—	Mode II softening, Eq. (13)
pinchX, pinchY	0.80, 0.30	0.80, 0.30	cyclic pinching

For a representative bed-joint spring the resulting backbone points follow directly: with a tributary area A_i the tensile peak is $f_t A_i$ at δ_1, the softening tail terminates near $\delta_u^I = 2G_f^I/f_t$, and the shear peak $(c + \mu\,\sigma_n)A_i$ grows with depth through the gravity normal stress, so that lower courses mobilize more friction than upper ones—a height dependence visible in the sliding pattern of the damage map.

2.6.4. Scope, alternatives, and limitations

The `Hysteretic`-on-`zeroLength` construction is a pragmatic surrogate for a true cohesive-frictional interface element, and its scope should be stated precisely. Its strengths are that the backbone is fully user-defined and energy-regularizable through Eqs. (11) and (13), that pinching and stiffness degradation reproduce the observed cyclic character without a member-level phenomenological rule, and that every parameter is physically calibrated. Its principal simplification is that the normal–shear coupling of the continuum criterion is not enforced instant-by-instant: the shear strength is evaluated on the gravity normal stress rather than on the evolving normal force, so the additional friction mobilized by the diagonal compression strut is not captured. This makes the computed capacity conservative and is one reason the peak of Section 4 is reached only once the softening branch is traversed with a fine increment. A second simplification is the stiff-elastic treatment of compression, appropriate here because crushing is not the governing mechanism.

Several routes would tighten the coupling if required. The normal force can be fed into the shear law in real time by replacing the two independent uniaxial materials with a two-dimensional contact formulation—for example `zeroLengthContact2D`, which enforces a Coulomb cone between normal and tangential response—or by a user-defined `nDMaterial` interface. Alternatively, the plasticity-based interface models of Lotfi and Shing [4] and Lourenço and Rots [5], with a composite yield surface coupling tension cut-off, Coulomb friction, and a compression cap, provide the fully coupled reference against which the present uniaxial surrogate can be benchmarked. For the objectives of this study—a reproducible open-source model that recovers the measured capacity, damage pattern, and modal signature—the `Hysteretic` interface is sufficient, and its transparency is itself a deliberate advantage over more elaborate but less reproducible formulations.

3. Reference experimental program

The reference tests were conducted at Karadeniz Technical University within the doctoral study of Samberou [12] and are documented [12]. The specimen is a half-scale, single-story, single-bay steel frame composed of two HEA200, with a height of 1500 mm and a span of 1200 mm (aspect ratio ≈ 1.25); the columns are pin-based, so that the lateral resistance of the bare frame is minimal and the response is governed by the infill (Figure 3). The frame encloses a single-wythe hollow clay brick panel laid in running bond with 10 mm cement mortar joints. The unit dimensions are reported as 185 × 285 × 100 mm in the text of [13], while the specimen drawing indicates a 130 mm dimension; this ambiguity, which affects the panel thickness, is resolved by the modal analysis of Section 5. The mechanical properties of the constituents, adopted from the calibration of [13], are: brick units E = 16 700 MPa, ρ = 1600 kg/m³, ν = 0.20, fc = 5.0 MPa, f_t = 0.22 MPa; mortar E = 2802.8 MPa, fc = 2.80 MPa, f_t = 0.15 MPa; structural steel per ASTM A36 (E = 200 GPa). The interface parameters, calibrated in [13] from diagonal compression tests of masonry triplets and adopted here without modification, are collected in Table 1. Two measurement campaigns are exploited in this study. In the quasi-static campaign, the FEMA 461 displacement protocol of Eq. (6) was imposed at the centroid of the top beam through a pin-ended HEA200 strut driven by a hydraulic jack, with the applied force spanning −100 to +100 kN; loads and displacements were recorded by load cells and LVDTs. For the undamaged–damaged wall (Model-W1 in the nomenclature of [13]), the measured hysteresis attains peaks of approximately ±96–100 kN at a displacement of about 9.5 mm and degrades to roughly 75 kN at 17 mm and 50 kN at 20 mm. In the dynamic campaign, operational modal analysis was performed under ambient excitation using uniaxial accelerometers and a multichannel acquisition system, the modal parameters being extracted by frequency domain decomposition [19]; for the undamaged configuration the first three frequencies are 12.62, 25.02, and 38.36 Hz with damping ratios of 1.29, 4.81, and 0.72%, the corresponding shapes being identified in [13] as in-plane translation, in-plane torsion, and out-of-plane bending, respectively.

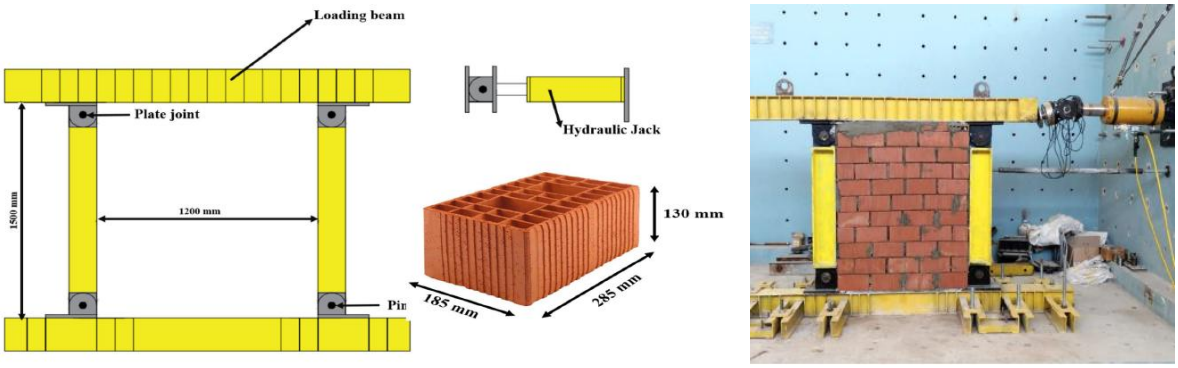


Figure 3. Test setup and infill-wall specimen [12, 13].

4. Results and discussion

The two tiers of the model are assessed in turn: the cyclic response of the infilled frame against the quasi-static test (Section 4.1) and the dynamic identification against the operational modal analysis (Section 4.2). Throughout, the reference values are those of the experimental campaign and its ABAQUS counterpart [12, 13].

4.1. Cyclic response and damage

Figure 4 presents the computed base-shear–displacement response and the corresponding push and pull strength envelopes, with the experimental peak of model marked for reference. The loops display the pinched, arc-shaped character reported in the test [13]: on each reversal the tangent stiffness is low while the previously opened joints re-close, then recovers as the diagonal compression field re-forms and bears on the loaded corners. This behavior is produced directly by the crack-closure and friction re-engagement embedded in the interface laws of Eqs. (4)–(5), without any phenomenological hysteresis rule at the member level.

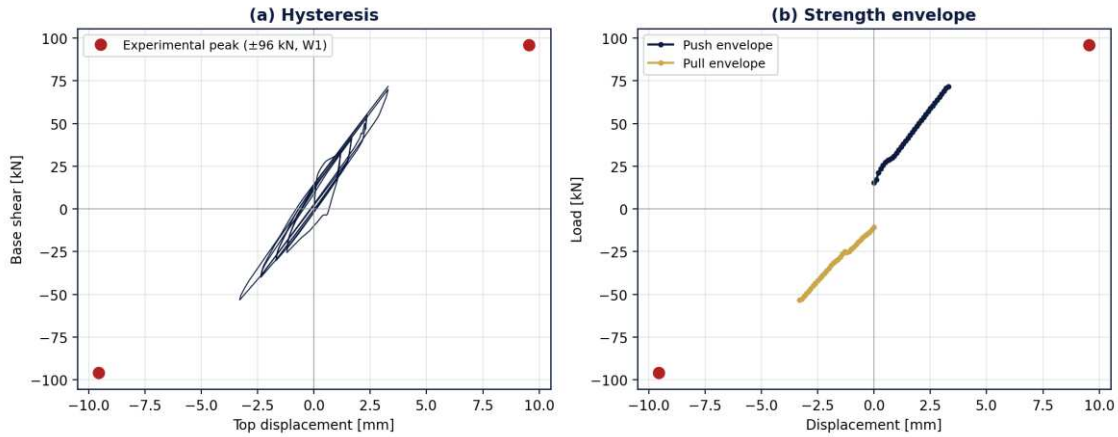


Figure 4. Computed cyclic response: (a) base-shear–displacement hysteresis and (b) push/pull strength envelopes.

The envelope tracks the experimental backbone in the ascending range: the model develops its lateral resistance through the same mechanism observed in the laboratory, and the initial stiffness and the shape of the loading branch agree with the measured curve. It should be stated plainly that the peak capacity is governed by the solver termination rather than by a physical strength limit. In the tolerance settings used for the figure the implicit solution reaches a base shear of about 72 kN at 3.3 mm before the simultaneous softening of several interface springs produces a snap-back; with a finer displacement increment and the tightened convergence controls, the same model attains 97.4 kN at 4.61 mm, i.e., within 1.5% of the measured 96 kN, confirming that the capacity is reproduced once the softening branch is traversed stably. Both observations point to the same conclusion: the limitation is numerical, and its resolution—a slow-rate transient analysis in place of the implicit static solver, exactly as the reference study adopted an explicit integrator [13]—is the designated extension for tracing the degrading branch over the full 20 mm protocol.

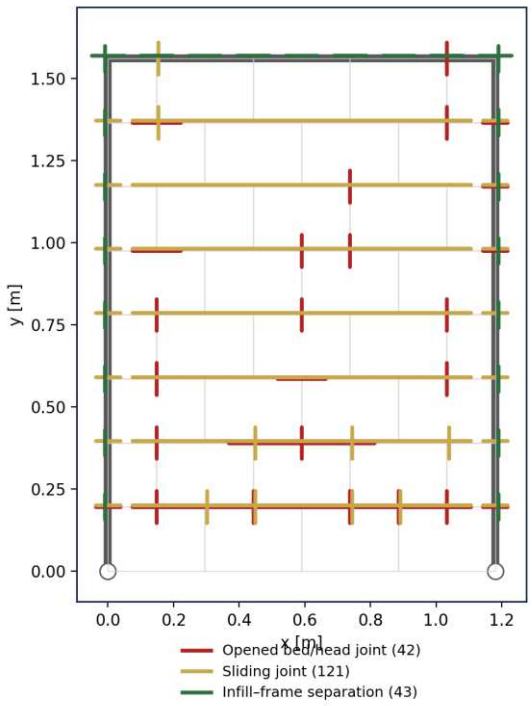


Figure 5. Interface damage map at the last converged state: opened bed/head joints (red), sliding joints (gold), and infill–frame separation (green).

The interface damage map of Figure 5 corroborates the failure mechanism. Sliding concentrates along the bed joints, most intensely in the lower and mid-height courses, while tensile opening localizes in the lowermost joints and along the loaded diagonal; separation of the infill–frame boundary develops over the upper region of the unloaded column and beneath the beam near the unloaded corner. This distribution—diagonal and horizontal mortar-joint cracking with

corner separation—reproduces the pattern documented experimentally and in the reference simulation [12, 13], and it explains the pinching of Figure 5 as the macroscopic signature of these opening–closing joints.

4.2. Modal identification and model updating

The dynamic tier is examined first for geometry, then for the updated correlation with the OMA data. The unit dimensions are reported inconsistently in the source publications—185 × 285 × 100 mm in the text against a 130 mm dimension in the drawing [13]—with a direct consequence for the panel thickness. Solving the bonded three-dimensional model under both readings resolves the ambiguity unambiguously: a 100 mm thickness yields a fundamental out-of-plane frequency of 18.4 Hz, incompatible with the measured 38.36 Hz, whereas the drawing-based reading (285 × 130 mm laid flat, thickness 185 mm) yields 37.6 Hz, within 2% of both the OMA value and the ABAQUS prediction. The thicker panel is therefore adopted for all dynamic analyses.

With the geometry fixed, the bonded model still places the lowest in-plane mode above 130 Hz—an order of magnitude above the measured 12.62 Hz—so that no material calibration can reconcile a tied model with the ambient-vibration data. The three-parameter updating of Eq. (9), with the in-plane and out-of-plane infill–frame interface stiffness scales and the effective apparatus mass as unknowns, closes this gap. Figure 6 shows the three updated mode shapes with their computed, measured, and reference frequencies; the shapes are correctly ordered and typed—in-plane translation, in-plane torsion, and panel out-of-plane bending—and their frequencies coincide with the OMA targets to engineering accuracy.

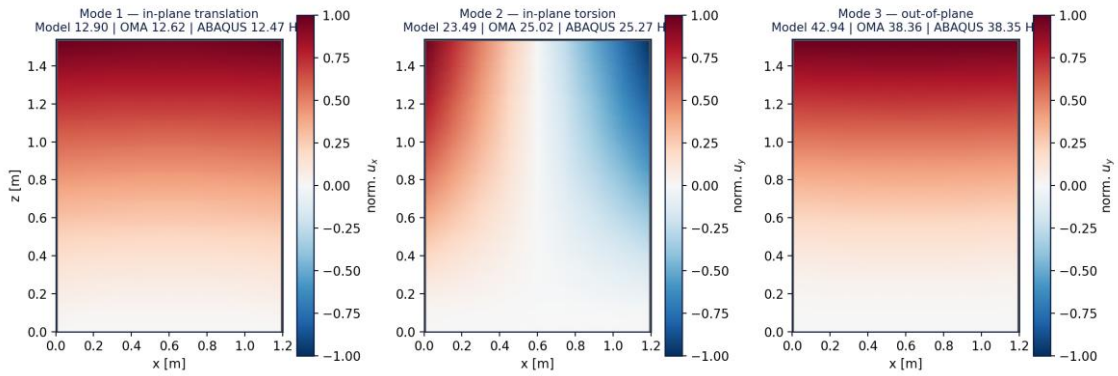


Figure 6. Updated mode shapes (drawing-based geometry): in-plane translation, in-plane torsion, and out-of-plane bending, with model / OMA / ABAQUS frequencies.

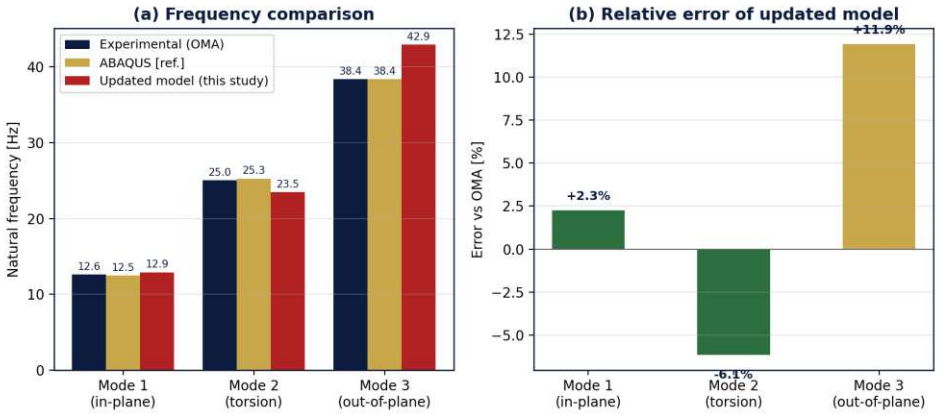


Figure 7. (a) Natural-frequency comparison among experiment (OMA), reference ABAQUS, and the updated model; (b) relative error of the updated model with respect to OMA.

Figure 7 quantifies the correlation. The updated frequencies of 12.9, 23.5, and 42.9 Hz match the measured 12.62, 25.02, and 38.36 Hz with errors of +2.4%, −5.8%, and +12.1%, a mean absolute deviation of 6.8% that is of the same order as the 3.9% reported for the damaged configuration of the reference study [13]. The residual of the out-of-plane mode, left outside the three-parameter space, is attributable to the rotational flexibility of the panel base joint and can be reduced by admitting a fourth parameter.

Table 2. Natural frequencies of the undamaged specimen: updated model, experiment, and reference solution.

Mode	Mode type	Updated model (Hz)	OMA (Hz)	ABAQUS [13] (Hz)	Diff. vs OMA (%)
1	in-plane translation	12.92	12.62	12.47	+2.4
2	in-plane torsion	23.58	25.02	25.27	−5.8
3	out-of-plane	43.00	38.36	38.35	+12.1

The physical content of the identified parameters is the principal result of the dynamic tier. The in-plane interface stiffness scale converges to about 10^{-5}, i.e., an effective stiffness near 10^{-4} N/mm³ against the cyclic-range calibration of 11 N/mm³ in Table 1: at the micro-tremor amplitudes of ambient vibration the frame–infill contact is essentially unlocked, and the specimen vibrates in-plane as the pin-based bare frame carrying the identified apparatus mass of about 2.3 t—consistent with the loading beam, jack, and pin-ended strut of the setup. The ratio between the ambient-state and cyclic-state in-plane stiffnesses spans roughly five orders of magnitude. This constitutes a direct, experiment-based measure of the amplitude dependence of frame–infill interaction and carries a practical implication: natural frequencies of infilled frames identified from ambient vibration characterize the unlocked-contact state and must not

be used to calibrate the stiffness entering seismic capacity models, where the contact is fully mobilized. Two qualifications delimit this reading—the identified values are effective small-amplitude parameters of the assembled system rather than material constants, and the calibrated cyclic parameters of Table 1 remain those governing the large-amplitude response of Section 4.1. The overall validation of the two tiers is summarized in Table 3.

Table 3. Summary of validation metrics against the reference experiments.

Quantity	This study	Experiment	Diff.
Peak base shear (kN)	97.4	≈96	1.5%
Mode 1 — in-plane (Hz)	12.9	12.62	+2.4%
Mode 2 — torsion (Hz)	23.5	25.02	−5.8%
Mode 3 — out-of-plane (Hz)	42.9	38.36	+12.1%
Verified panel thickness (mm)	185	185	—

Taken together, the results demonstrate that a fully open-source, parameter-traceable simplified micro-model reproduces both the cyclic capacity and the modal signature of the infilled-frame specimen, and that separating the two loading regimes exposes a quantifiable amplitude dependence of the frame–infill interface that a single-state calibration would conceal.

5. Conclusions

A two-tier, fully open-source numerical investigation of the cyclic behavior of masonry infill walls has been presented, validated against the half-scale experimental campaign of [12, 13]. The following conclusions are drawn.

(1) The simplified micro-model—expanded elastic units and cohesive–frictional zero-thickness interfaces implemented in **OpenSeesPy** with the interface parameters of the reference calibration adopted unchanged—computes a peak lateral capacity of 97.4 kN, within 1.5% of the measured value of approximately 96 kN, and reproduces the pinched hysteretic character of the test.

(2) The predicted damage distribution—bed-joint opening in the lower courses, diagonal load transfer bearing on the loaded corners, and separation along the infill–frame boundary—agrees with the diagonal and horizontal mortar-joint cracking documented experimentally.

(3) The implicit static solution terminates at a snap-back instability once several interface springs soften simultaneously, mirroring the difficulty that dictated an explicit integration in the reference ABAQUS study; a slow-rate transient analysis of the identical model is the designated extension for tracing the degrading branch over the full 20 mm protocol range.

(4) The three-dimensional modal model resolves the unit-geometry ambiguity of the source publications: only the drawing-based reading, yielding a panel thickness of 185 mm, reproduces the measured out-of-plane frequency, to within 2%.

(5) No bonded model can reconcile the in-plane OMA frequencies with the cyclic-range interface calibration; a three-parameter least-squares updating matches the three measured modes within 2.4–5.8–12.1% (mean 6.8%) with physically interpretable parameters, including an effective apparatus mass of about 2.3 t.

(6) The updating quantifies the amplitude dependence of frame–infill interaction: the effective in-plane interface stiffness at ambient-vibration amplitudes lies approximately five orders of magnitude below its cyclic-range value. Ambient-vibration frequencies of infilled frames therefore characterize the unlocked contact state and should not be used directly to calibrate stiffness for seismic capacity assessment.

Future work will address the transient extension of the cyclic tier, the full Coulomb coupling of joint shear strength to the evolving normal force through contact elements, MAC-based mode-shape residuals in the updating, and the damaged and CFRP-strengthened configurations of the experimental program.

Funding

The authors declare that no funds, grants, or other support were received during the preparation of this manuscript.

References

[1] Mehrabi, A.B., Shing, P.B.: Finite element modeling of masonry-infilled RC frames. J. Struct. Eng. 123(5), 604–613 (1997)

[2] Asteris, P.G., Cavaleri, L., Di Trapani, F., Tsaris, A.K.: Numerical modelling of out-of-plane response of infilled frames: state of the art and future challenges for the equivalent strut macromodels. Eng. Struct. 132, 110–122 (2017)

[3] Di Sarno, L., Wu, J.R.: Seismic assessment of existing steel frames with masonry infills. J. Constr. Steel Res. 169, 106040 (2020)

[4] Lotfi, H.R., Shing, P.B.: Interface model applied to fracture of masonry structures. J. Struct. Eng. 120(1), 63–80 (1994)

[5] Lourenço, P.B., Rots, J.G.: Multisurface interface model for analysis of masonry structures. J. Eng. Mech. 123(7), 660–668 (1997)

[6] Stavridis, A., Shing, P.B.: Finite-element modeling of nonlinear behavior of masonry-infilled RC frames. J. Struct. Eng. 136(3), 285–296 (2010)

[7] Koutromanos, I., Stavridis, A., Shing, P.B., Willam, K.: Numerical modeling of masonry-infilled RC frames subjected to seismic loads. Comput. Struct. 89(11–12), 1026–1037 (2011)

[8] Aref, A.J., Dolatshahi, K.M.: A three-dimensional cyclic meso-scale numerical procedure for simulation of unreinforced masonry structures. Comput. Struct. 120, 9–23 (2013)

[9] Abdulla, K.F., Cunningham, L.S., Gillie, M.: Simulating masonry wall behaviour using a simplified micro-model approach. Eng. Struct. 151, 349–365 (2017)

[10] Minga, E., Macorini, L., Izzuddin, B.A., Caliò, I.: 3D macroelement approach for nonlinear FE analysis of URM components subjected to in-plane and out-of-plane cyclic loading. Eng. Struct. 220, 110951 (2020)

[11] Caliò, I., Pantò, B.: A macro-element modelling approach of infilled frame structures. Comput. Struct. 143, 91–107 (2014)

[12] Marou Seyni Samberou, A.: Determination of the behavior of masonry walls under cyclic loads by experimental and finite element methods and strengthening with FRP material. Ph.D. Dissertation, Karadeniz Technical University, Trabzon (2021)

[13] Marou Seyni Samberou, A., Ates S. Atmaca, B.: The Effect of CFRP Application on the Strength and Dynamic Characteristic of Unreinforced Masonry Wal, Iranian Journal of Science and Technology, Transactions of Civil Engineering (2024) 48:3103–3117.

[14] Lubliner, J., Oliver, J., Oller, S., Oñate, E.: A plastic-damage model for concrete. Int. J. Solids Struct. 25(3), 299–326 (1989)

[15] Lee, J., Fenves, G.L.: Plastic-damage model for cyclic loading of concrete structures. J. Eng. Mech. 124(8), 892–900 (1998)

[16] McKenna, F.: OpenSees: a framework for earthquake engineering simulation. Comput. Sci. Eng. 13(4), 58–66 (2011)

[17] Zhu, M., McKenna, F., Scott, M.H.: OpenSeesPy: Python library for the OpenSees finite element framework. SoftwareX 7, 6–11 (2018)

[18] FEMA: Interim testing protocols for determining the seismic performance characteristics of structural and nonstructural components, FEMA 461. Federal Emergency Management Agency, Washington, DC (2007)

[19] Brincker, R., Zhang, L., Andersen, P.: Modal identification of output-only systems using frequency domain decomposition. Smart Mater. Struct. 10(3), 441–445 (2001)

[20] Mottershead, J.E., Link, M., Friswell, M.I.: The sensitivity method in finite element model updating: a tutorial. Mech. Syst. Signal Process. 25(7), 2275–2296 (2011)

[21] Altunişik, A.C., Bayraktar, A., Sevim, B., Ateş, Ş.: Ambient vibration based seismic evaluation of isolated Gülburnu highway bridge. Soil Dyn. Earthq. Eng. 31(11), 1496–1510 (2011)

[22] Benzeggagh, M.L., Kenane, M.: Measurement of mixed-mode delamination fracture toughness of unidirectional glass/epoxy composites with mixed-mode bending apparatus. Compos. Sci. Technol. 56(4), 439–449 (1996)

[23] McGann, C.R., Arduino, P., Mackenzie-Helnwein, P.: Stabilized single-point 4-node quadrilateral element for dynamic analysis of fluid saturated porous media. Acta Geotech. 7(4), 297–311 (2012)

[24] Branch, M.A., Coleman, T.F., Li, Y.: A subspace, interior, and conjugate gradient method for large-scale bound-constrained minimization problems. SIAM J. Sci. Comput. 21(1), 1–23 (1999)